applied sciences

MDPI

Article

Thermal Stability and Tuning of Thermoelectric Properties of $Ag_{1-x}Sb_{1+x}Te_{2+x}$ ($0 \leq x \leq 0.4$) Alloys

Paweł Wyżga [1,2,3,*], Igor Veremchuk [3,*], Ulrich Burkhardt [3], Paul Simon [3], Yuri Grin [3] and Krzysztof T. Wojciechowski [2]

1 Institut für Experimentelle Physik, TU Bergakademie Freiberg, Leipziger Str. 23, 09599 Freiberg, Germany
2 Thermoelectric Research Laboratory, Faculty of Materials Science and Ceramics, AGH University of Science and Technology, A. Mickiewicza Av. 30, 30-059 Krakow, Poland; wojciech@agh.edu.pl
3 Max-Planck-Institut für Chemische Physik fester Stoffe, Nöthnitzer Str. 40, 01187 Dresden, Germany; ulrich.burkhardt@cpfs.mpg.de (U.B.); paul.simon@cpfs.mpg.de (P.S.); grin@cpfs.mpg.de (Y.G.)
* Correspondence: pawel.wyzga@physik.tu-freiberg.de (P.W.); igor.veremchuk@cpfs.mpg.de (I.V.); Tel.: +49-351-46464000 (P.W.)

Received: 14 November 2017; Accepted: 25 December 2017; Published: 4 January 2018

Abstract: Introduction of nonstoichiometry to $AgSbTe_2$-based materials is considered to be an effective way to tune thermoelectric properties similarly to extrinsic doping. To prove this postulate, a systematic physicochemical study of the $Ag_{1-x}Sb_{1+x}Te_{2+x}$ alloys ($0 \leq x \leq 0.4$) was performed. In order to investigate the influence of the cooling rate after synthesis on phase composition and thermoelectric performance, slowly cooled and quenched $Ag_{1-x}Sb_{1+x}Te_{2+x}$ alloys (x = 0; 0.1; 0.17; 0.19; 0.3; 0.4) were prepared. Single-phase material composed of the β phase (NaCl structure type) was obtained for the quenched x = 0.19 sample only. The other alloys must be regarded as multi-phase materials. The cooling rate affects the formation of the phases in the Ag-Sb-Te system and influences mainly electronic properties, carrier mobility and carrier concentration. The extremely low lattice thermal conductivity is an effect of the mosaic nanostructure. The maximal value of the figure of merit ZT_{max} = 1.2 is observed at 610 K for the slowly cooled multi-phase sample $Ag_{0.9}Sb_{1.1}Te_{2.1}$. Thermoelectric properties are repeatedly reproducible up to 490 K.

Keywords: thermoelectric properties; $Ag_{1-x}Sb_{1+x}Te_{2+x}$; thermodynamic stability; nanostructure

1. Introduction

Chalcogenides that crystallize in the NaCl structure type ($Fm\bar{3}m$), e.g., PbTe, PbSe or SnTe, belong to the best thermoelectric (TE) materials [1]. Numerous studies, concerning the TE performance of $AgSbTe_2$-alloys with various dopants, reported very large values of TE figure of merit $ZT > 1.3$ [2–6]. That is mainly due to the extremely low thermal conductivity of the material in the range of 0.5–0.7 $W \cdot m^{-1} \cdot K^{-1}$ [7–9]. However, their potential application in TE devices is limited due to thermodynamic instability in the working temperature range (300–600 K) [3,10–12].

The origin of specific transport properties of Ag-Sb-Te-based materials is thought to be connected with their local crystal structure. $AgSbTe_2$ crystallizes in the NaCl structure type, where Ag and Sb atoms randomly occupy the same Wyckoff position 4*a* and Te atoms are at 4*b* sites [13,14]. However, the existence of highly complex local atomic ordering was suggested due to notable discrepancies in the atomic properties of Ag and Sb, e.g., atomic radii, electronic structure or oxidation state [13,14]. On the basis of either Rietveld refinements [15,16] or ab initio theoretical calculations [17,18], different possible superstructures were proposed with cubic (space group $Fd\bar{3}m$), rhombohedral ($R\bar{3}m$) or tetragonal ($P4/mmm$ or $I4_1/amd$) symmetry.

Thermodynamic properties of Ag-Sb-Te alloys were investigated by several groups. Pseudobinary phase diagrams of the Sb_2Te_3-Ag_2Te system were elaborated separately in [10,19] (Figure 1).

The composition of each alloy within the diagram is described by the chemical formula $Ag_{1-x}Sb_{1+x}Te_{2+x}$ ($-1 \leq x \leq 1$). A phase with the nominal composition of $AgSbTe_2$ does not exist. To emphasize the fact that the $AgSbTe_2$ formula relates only to a nominal composition, $Ag_{1.0}Sb_{1.0}Te_{2.0}$ notation was used in the whole text below. In fact, the only thermodynamically stable ternary phase in this system is the β phase ($Ag_{1-x}Sb_{1+x}Te_{2+x}$, $0.08 < x < 0.41$ [10]), which crystallizes in the NaCl structure type. However, earlier reports differ about the temperature and compositional region of the β phase [10,19]. Further investigations of the Ag-Sb-Te ternary system confirmed that the β phase is only stable in a limited temperature range (633 K < T < 847 K) and it decomposes into α (solid solution of Ag in Sb_2Te_3) and ε (solid solution of Sb in β-Ag_2Te) phases below 633 K [11,12,20]. The decomposition process was additionally confirmed by temperature-dependent X-ray diffraction analysis [21] and electrochemical measurements [22]. The influence of thermal treatment on TE properties of the $Ag_{1.0}Sb_{1.0}Te_{2.0}$ alloy is easily recognizable. In a previous work, we have noticed significant changes in Seebeck coefficient and electrical conductivity during measurements that were attributed to chemical and microstructural changes of the investigated materials [12].

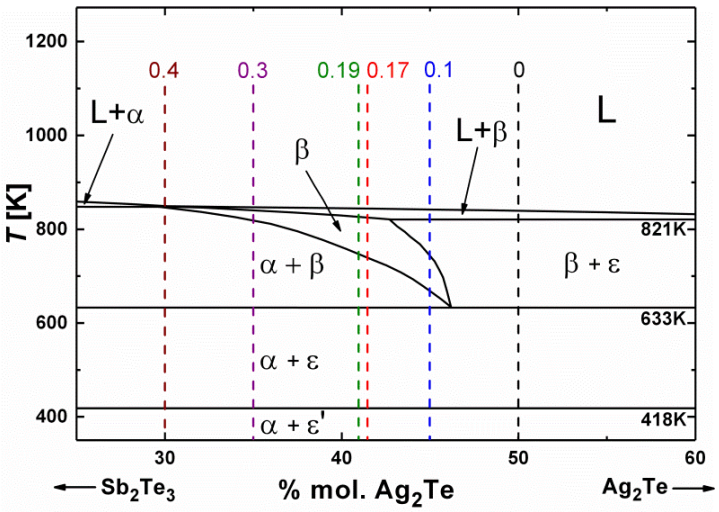

Figure 1. Part of the phase diagram of the Sb_2Te_3–Ag_2Te pseudobinary system based on data of [10]. Dashed lines indicate the nominal compositions x of synthesized samples $Ag_{1-x}Sb_{1+x}Te_{2+x}$; α—solid solution of Ag in Sb_2Te_3, β—$Ag_{1-x}Sb_{1+x}Te_{2+x}$ ($0.08 < x < 0.41$), ε—solid solution of Sb in Ag_2Te.

In the earliest report of electrical properties of $Ag_{1-x}Sb_{1+x}Te_{2+x}$ alloys [23], samples with a gradual change of phase and chemical composition were obtained. It was shown that alloys with $0 < x < 0.2$ possess the most prominent power factor $PF = 5 \times 10^{-4}$ W·m^{-2}·K^{-2} at room temperature (RT). Single-phase alloy with the nominal composition $Ag_{0.875}Sb_{1.125}Te_2$ (not included in the pseudobinary Sb_2Te_3-Ag_2Te system) was characterized by $PF = 2 \times 10^{-5}$ W·m^{-2}·K^{-2} at RT [24]. High TE performance of $Ag_{1-x}Sb_{1+x}Te_{2+x}$ alloys (ZT = 1.2–1.4 at 600 K) with x >0.25 was reported in [25,26]. There is also a strong conviction in the literature that a small change in Ag/Sb ratio effectively enhances electrical properties, due to the formation of vacancies at the Ag/Sb site, without altering thermal conductivity [25,27,28].

One can notice that systematic studies about the physicochemical properties of $Ag_{1-x}Sb_{1+x}Te_{2+x}$ alloys ($0 < x < 0.4$) are still missing. Therefore, we decided to answer two questions: (i) what is the real stability range of the β phase within the pseudobinary Sb_2Te_3-Ag_2Te system, (ii) whether tuning of thermodynamic stability and TE performance is indeed possible by deviating composition from the stoichiometric $Ag_{1.0}Sb_{1.0}Te_2$. This study also includes a thorough analysis of the micro- and nanostructure of nonstoichiometric $Ag_{1-x}Sb_{1+x}Te_{2+x}$ alloys. Additionally, we investigated the influence of thermal treatment on thermodynamic stability and TE performance of alloys. We synthesized two

series of samples: (1) slowly cooled and (2) quenched sets. Although our experiments and following conclusions concern the Sb_2Te_3-Ag_2Te pseudobinary system only, some of them can be applicable to the Ag-Sb-Te ternary system as well.

2. Experimental

2.1. Preparation

Two series of $Ag_{1-x}Sb_{1+x}Te_{2+x}$ alloys (x = 0; 0.1; 0.17; 0.19; 0.3; 0.4) were synthesized. Nominal compositions x are presented in Figure 1. All manipulations were performed in an argon-filled glovebox. Small granules and pieces of elements Ag (99.9%, Alfa Aesar, Thermo Fisher (Kandel) GmbH, Karlsruhe, Germany), Sb (99.9999%, Alfa Aesar, Thermo Fisher (Kandel) GmbH, Karlsruhe, Germany) and Te (99.999%, Chempur, Karlsruhe, Germany) were weighted and placed in glassy-carbon crucibles with lids. To reduce evaporation and oxidation of materials, at least 50% of the crucible volume was filled and crucibles were placed in welded tantalum tubes (Ar atmosphere), sealed in quartz ampoules. Thermal treatment was carried out at 1023 K for 4 h. Then, the ampoules were slowly cooled down to room temperature in the furnace, with a starting rate 2.4 K·min^{-1} (1st series). Obtained ingots were crushed and half of each specimen was sealed again in quartz ampoules, under a vacuum of approximately 10^{-2} Pa. After annealing at 1023 K for 1 h, ampoules were quenched in iced water (2nd series). In order to refine the lattice parameter of equilibrated β phase, each sample was additionally annealed at 723 K for 1.5 months (quartz ampoules, vacuum of 10^{-2} Pa) followed by quenching.

2.2. Powder X-ray Diffraction, Thermal Analysis and Chemical Analysis

Structural characterization was carried out by powder X-ray diffraction (PXRD, Huber G670 Guinier camera, Cu $K_{\alpha 1}$ radiation, λ = 1.54056 Å, $\Delta 2\theta$ = 0.005°, HUBER Diffraktionstechnik GmbH & Co., KG, Rimsting, Germany). Data were collected at room temperature using LaB_6 (NIST, 660a) as an internal standard. An experimental position of each reflection was corrected by comparison with standard, and lattice parameters of the β phase were calculated from least-squares refinement using WinCSD software [29]. Absence of C, N, O impurities was verified by elemental analysis (TCH600, C200, Leco, St. Joseph, MI, USA) and inductively coupled plasma optical emission spectroscopy (ICP-OES 5100, Agilent Technologies, Santa Clara, CA, USA). Thermogravimetry and differential thermal analysis experiments (TG-DTA: STA 449F3, Al_2O_3 crucibles; DTA: STA 409C/CD, SiO_2 ampoules, Netzsch GmbH & Co., Selb, Germany ; heating rate: 5/10 K·min^{-1}) were performed to identify phase transitions and to detect Ag_2Te impurities.

2.3. Metallography and Scanning Electron Microscopy

Samples for metallographic investigation were embedded in a conductive resin, polished with SiC abrasive paper with different grit (i.e., 1200, 2400, and 4000) and then with a diamond polishing belt (particle size 0.25 µm), applying dry hexane as a lubricant under ambient conditions. Microstructure analysis of polished samples was carried out by using optical microscopy (Axioplan 2, bright field or polarized light, Carl Zeiss AG, Oberkochen, Germany) and scanning electron microscopy (SEM, Philips/FEI XL30, LaB_6 cathode, FEI Technologies Inc., Hillsboro, OR, USA) with integrated energy dispersive X-ray spectrometer (EDXS,Quantax 400, XFlash 6|30 silicon drift detector, Bruker Corporation, Billerica, MI, USA).

2.4. High-Resolution Transmission Electron Microscopy

The atomic structure of single-phase $Ag_{0.81}Sb_{1.19}Te_{2.19}$ alloy was analyzed by means of high-resolution transmission electron microscopy (HRTEM) using FEI Tecnai F30-G2 microscope (field-emission gun at an acceleration voltage of 300 kV; point resolution and information limit were amounted to 1.9 Å and 1.2 Å, respectively, FEI Technologies Inc., Hillsboro, OR, USA) and

selected area electron diffraction (SAED). The microscope was equipped with a slow-scan CCD camera (MultiScan, 2 k × 2 k pixels; Gatan Inc., Pleasanton, CA, USA) and EDXS spectrometer. The powdered sample was dispersed in methanol and several drops of the solution were loaded on carbon coated copper grid (Quantifoil S7/2, 100-mesh hexagonal, 2 nm carbon film, Quantifoil Micro Tools, Jena, Germany). The grid was transferred to the microscope after complete dryness. Analysis of the TEM images was performed using Digital Micrograph software (Version 2, Gatan Inc., Pleasanton, CA, USA). It includes fast Fourier transform (FFT)/inverse fast Fourier transform (IFFT), filtering and brightness/contrast corrections.

2.5. Spark Plasma Sintering and Thermoelectric Properties

High-temperature TE properties were determined in the temperature range of 298–610 K. Samples for TE measurements were manually ground in an agate mortar and compacted using the spark plasma sintering apparatus placed in an argon-filled glove-box (515ET Sinter Lab, Fuji Electronic Industrial Co., Ltd., Tsurugashima Saitama, Japan, 753 K, 5 min, 40 MPa, graphite dies [30]). Obtained cylindrical pellets (φ = 10 mm) were used for studies of thermal properties. Thermal diffusivity α_d was measured by laser flash analysis (LFA 457 MicroFlash, HgCdTe detector, Netzsch GmbH & Co., Selb, Germany) under helium flow. Densities ρ of the samples (higher than 95% of theoretical density) were determined using an immersion technique with ethanol as a medium. Specific heat capacity c_p was evaluated from Dulong-Petit law and the thermal conductivity λ was calculated as

$$\lambda = \alpha_d \cdot \rho \cdot c_p \quad (1)$$

Samples, after LFA measurements, were cut into bars (~8 × 2 × 2 mm) for electronic-transport measurements and low temperature tests. The Seebeck coefficient α and electrical conductivity σ were determined simultaneously using differential method and the DC four-point probe method, respectively (ZEM-3, Ulvac-Riko, Munich, Germany). The Hall effect in single- or near-single-phase samples (x = 0.17 and 0.19) was measured with a six-point AC method in a physical property measurement system (PPMS, 2–350 K, Quantum Design Inc., San Diego, CA, USA), with magnetic fields up to 9 T. Carrier concentration p and mobility μ were calculated as

$$p = (e \cdot R_H)^{-1}, \quad (2)$$

$$\mu = \sigma \cdot (p \cdot e)^{-1}, \quad (3)$$

where R_H is the Hall coefficient (cm^{-3}) and e is the electron charge equals 1.602 × 10^{-19} C. Thermoelectric figure of merit ZT was calculated as

$$ZT = \alpha^2 \cdot \sigma \cdot \lambda^{-1} \cdot T \quad (4)$$

where T is absolute temperature (K). According to manufacturer's data, we estimated measurement errors $s(\lambda)$, $s(\sigma)$, $s(\alpha)$, and $s(ZT)$ equal 5%, 10%, 10% and 20% respectively.

3. Results & Discussion

3.1. Structural and Thermal Properties

Phase composition of $Ag_{1-x}Sb_{1+x}Te_{2+x}$ alloys was verified using PXRD experiments coupled with DTA thermal analysis. PXRD patterns of as-cast samples are presented in Figure 2. Main reflections were assigned to the β phase with NaCl-type crystal structure. The presence of small amounts of secondary phases is revealed. The slow cooling process does not allow obtaining single-phase materials in the whole analyzed compositional region, in agreement with the phase diagram [10] (Figure 1). The existence of Ag_2Te and Sb_2Te_3 precipitations after slow cooling, especially in samples from the compositional region of the β phase, is the result of the eutectoid decomposition of the latter in the

reaction $\beta \leftrightarrow \alpha + \varepsilon$ at 633 K [10]. However, the rate of this process is so small that even slow cooling can impede it. PXRD analysis of samples after quenching reveals that this procedure effectively minimizes the quantity of secondary phases and in the case of alloys with x = 0.19 and 0.17 (compositions from homogeneity region of the β phase) enables us to prepare single-phase materials (Figure 2).

The strongest reflection from Ag_2Te (2θ = 31.06°) can be overlooked and alloys with nominal compositions of x = 0.1 and x = 0 can be considered as single-phase materials. Therefore, DTA analysis was performed to verify our PXRD data (Figure S1). Each expected thermal effect corresponding to the β phase was detected, together with a small endothermic peak at 418 K associated with the polymorphic phase transition of Ag_2Te (Figure S1a, Table S1). A tiny endothermic effect was found at 693 K, which was ascribed to the incongruent melting of Ag_5Te_3 [31]. However, no reflections of that phase are visible in PXRD pattern (Figure 2). The concentration of this phase seems to be below the detection limit of PXRD analysis. The results prove that rate of the decomposition of the β phase is low and impurities are present in the form of the mixture of Ag-Te phases, in agreement with our previous investigations [12]. Thermal analysis of the slowly cooled x = 0.19 sample shows only peaks associated with decomposition and incongruent melting of the β phase (Figure S1b).

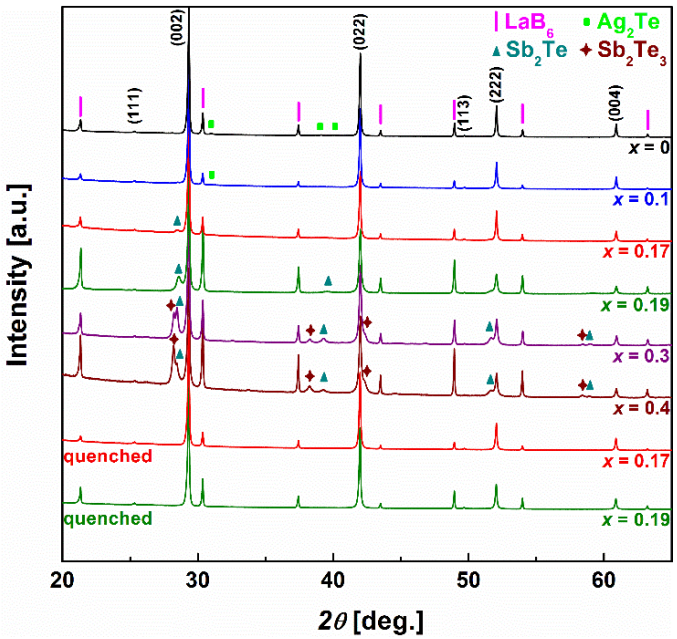

Figure 2. Powder XRD patterns of slowly cooled $Ag_{1-x}Sb_{1+x}Te_{2+x}$ samples. For comparison, patterns of samples with x = 0.17 and 0.19 after quenching are shown in the bottom; LaB_6 was used as an internal standard.

Lattice parameters of the β phase for $Ag_{1-x}Sb_{1+x}Te_{2+x}$ alloys are presented in Figure 3.

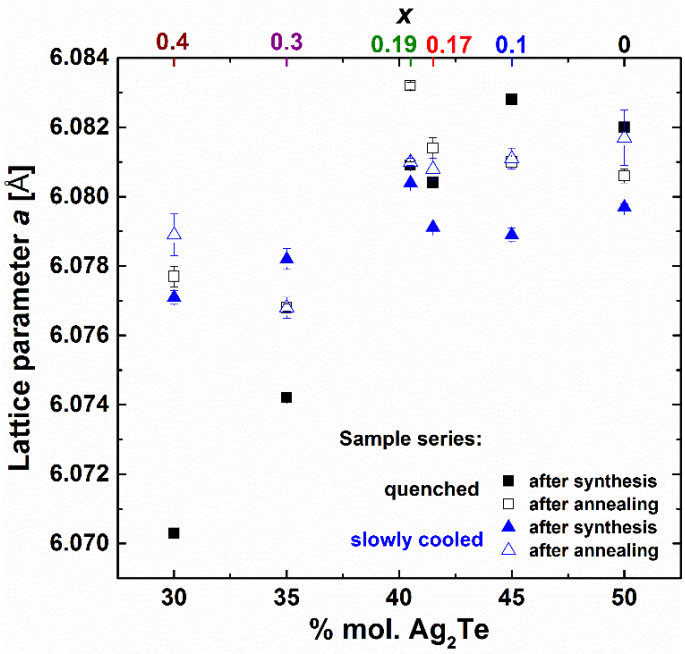

Figure 3. Lattice parameters of the β phase as a function of nominal composition.

Assuming no interstitials and anti-site defects (Ag/Sb at 4*a* sites and Te at 4*b* sites only), increase of x ($0 < x < 1$) in the formula $Ag_{1-x}Sb_{1+x}Te_{2+x}$ enhances the concentration of vacancies at 4*a* site and reduces the lattice parameter of the β phase. For the non-annealed samples, the lattice parameter increases with Ag-content for the lower silver concentrations and remains almost constant for more than 45 mol.% of Ag_2Te. After annealing, the lattice parameter practically does not change with concentration (Figure 3). This behavior suggests a wider homogeneity range of the β phase at elevated temperatures. Particular temperature treatment (cooling rate, annealing) of Ag-Sb-Te samples results in the formation and certain ordering of vacancies at 4*a* crystallographic sites. Kinetic hindering of the formation and decomposition reaction of the β phase at 633 K inhibits the complete equilibration of the samples, even after long term annealing. Small discrepancies in values, between respective samples after annealing (from different series), are visible and show the importance of the thermal history of Ag-Sb-Te alloys. The above discussion is focused on the Sb_2Te_3-Ag_2Te cross-section. However, the real homogeneity region of the β phase in the ternary Ag-Sb-Te system can be more complex and situated out of the Sb_2Te_3-Ag_2Te cross-section, what was partially shown in [11].

3.2. Microstructures

The microstructures of $Ag_{1-x}Sb_{1+x}Te_{2+x}$ alloys can be divided into three groups (Figure 4). Slowly cooled samples with the highest concentration of Sb, x = 0.4 and x = 0.3 (Figure 4b and Figure S3), show an evident Widmanstätten-like microstructure [23,25,32]. The specific pattern is caused by crystallization of elongated grains of Sb_2Te_3 and Sb_2Te in matrix of the β phase (Figure 4b, Figures S2a and S3). Shorter time of solidification inhibits straightforward crystallization of Sb-Te phases. Thus, the Widmanstätten-like pattern is not formed after quenching (Figure 4a and Figure S3a,c). Chemical compositions of the β phase after different cooling processes are comparable (Table 1).

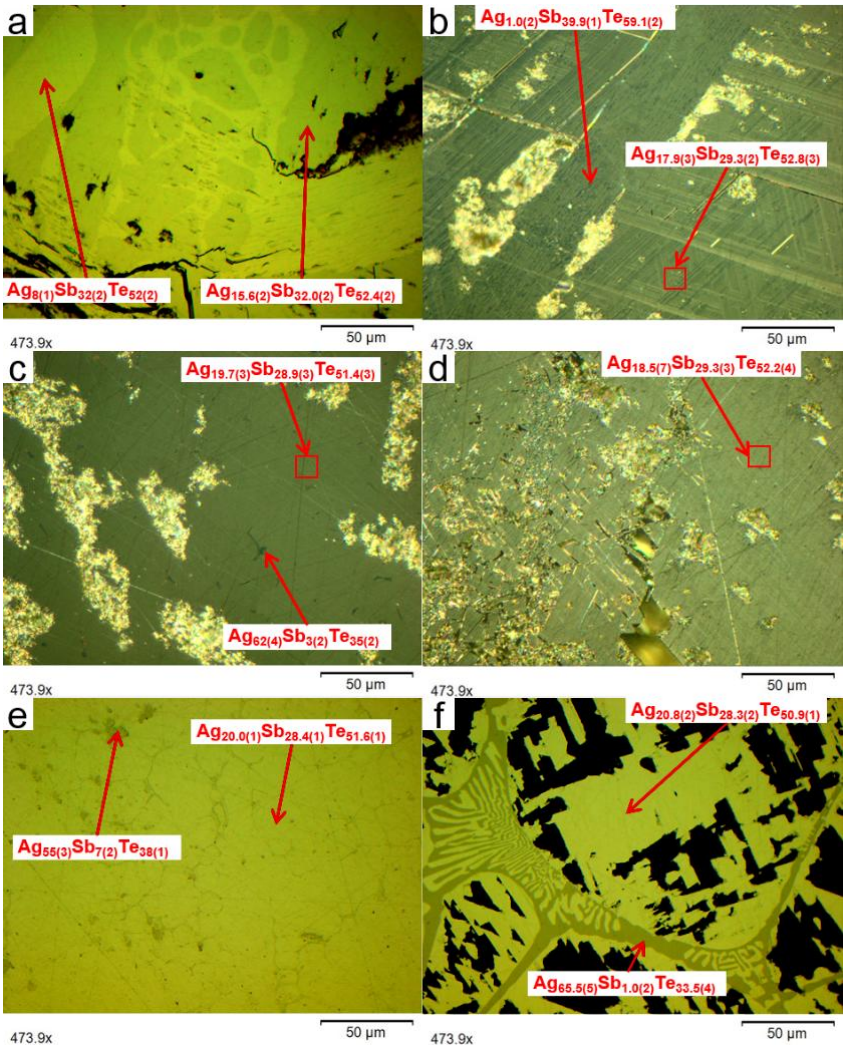

Figure 4. Optical polarized light (**b**–**d**) and bright field (**a**,**e**,**f**) micrographs of: (**a**,**b**) $x = 0.4$, (**c**,**d**) $x = 0.17$ and (**e**,**f**) $x = 0.1$ alloys; quenched samples—(**a**,**c**,**e**) and slowly cooled samples—(**b**,**d**,**f**). Chemical compositions of phases are given according to EDXS analysis.

A second group of alloys, $x = 0.19$ and $x = 0.17$, is characterized by a near-single or single-phase microstructure (Figure 4c,d and Figure S2b,c). A small amount of Sb-Te precipitations result in barely visible Widmanstätten-like pattern in alloys after slow cooling (Figure 4d, Figures S2b and S4b). An increase of cooling rate inhibits the precipitation of the secondary phases ($x = 0.19$, Figures S2c and S4a). Quenched $x = 0.17$ sample contains vestigial inclusions of Ag_2Te, undetectable by PXRD (Figure 4c and Figure S4c).

A third type of microstructure: lamellar, pearlite-like precipitations of Ag_2Te in the β phase matrix was observed in slowly cooled alloys with the highest content of Ag ($x = 0$; 0.1; Figure 4f and Figure S4f). The cooling rate strongly affects the morphology of those grains, which are much thinner after quenching (on the level of 1 µm, Figure 4e and Figure S4e). The chemical composition of the matrix in the analyzed alloys is almost the same, suggesting this to be the limiting composition of β-phase-region. Additional annealing during the SPS procedure and LFA measurement does not influence the chemical composition of the matrices; they remain practically unchanged (Table 1). However, a slight increase of the impurity concentration and modification of the microstructure is visible as the result of the slow decomposition of the β phase. Detailed discussion of the chemical compositions is given in supplementary information (Section 3).

Table 1. Chemical composition of the β phase in $Ag_{1-x}Sb_{1+x}Te_{2+x}$ alloys, according to EDXS analysis.

x	Nominal Composition (at. %)	Composition of the β Phase according to EDXS (at. %)		
		After Quenching	After Slow Cooling	After LFA
0.4	$Ag_{13.6}Sb_{31.8}Te_{54.6}$	$Ag_{15.6(2)}Sb_{32.0(2)}Te_{52.4(2)}$	$Ag_{17.9(3)}Sb_{29.3(2)}Te_{52.8(3)}$	$Ag_{16.6(8)}Sb_{30.8(5)}Te_{52.6(3)}$
0.3	$Ag_{16.3}Sb_{30.2}Te_{53.5}$	$Ag_{14.9(5)}Sb_{31(1)}Te_{54.1(9)}$	$Ag_{15.1(8)}Sb_{31.4(5)}Te_{53.5(3)}$	$Ag_{17.5(2)}Sb_{29.7(1)}Te_{52.8(2)}$
0.19	$Ag_{19.0}Sb_{29.0}Te_{52.0}$	$Ag_{18.9(2)}Sb_{29.5(2)}Te_{51.6(2)}$	$Ag_{18.8(3)}Sb_{29.5(2)}Te_{51.7(1)}$	$Ag_{18.2(6)}Sb_{30.0(8)}Te_{51.8(8)}$
0.17	$Ag_{20.0}Sb_{28.0}Te_{52.0}$	$Ag_{19.7(3)}Sb_{28.9(3)}Te_{51.4(3)}$	$Ag_{18.5(7)}Sb_{29.3(3)}Te_{52.2(4)}$	$Ag_{20.1(6)}Sb_{28.2(4)}Te_{51.8(2)}$
0.1	$Ag_{22.0}Sb_{26.8}Te_{51.2}$	$Ag_{20.0(1)}Sb_{28.4(1)}Te_{51.6(1)}$	$Ag_{20.8(2)}Sb_{28.3(2)}Te_{50.9(1)}$	$Ag_{18.3(4)}Sb_{27.9(4)}Te_{53.8(4)}$
0	$Ag_{25.0}Sb_{25.0}Te_{50.0}$	$Ag_{21.0(3)}Sb_{28.0(3)}Te_{51.0(2)}$	$Ag_{20.6(1)}Sb_{28.2(3)}Te_{51.2(2)}$	$Ag_{21.1(1)}Sb_{27.8(3)}Te_{51.1(3)}$

3.3. Thermoelectric Properties

The electrical properties were measured in several heating-cooling cycles from *RT* to 610 K. During subsequent measurement cycles, the decomposition process occurs and both phase composition and microstructure differ from the starting ones. This effect is discussed later. Here, we present results of the first heating cycle only. Each sample show metallic $\sigma(T)$ dependence up to 500 K (Figure 5a). The highest values of electrical conductivity were observed for Sb-rich alloys with a notable concentration of Sb-Te impurities (x = 0.3, 0.4), independent of the cooling rate. The conductivity is higher than 10^5 S·m^{-1} at *RT* and resembles values typical for the Sb_2Te_3 phase ($1.5 - 2 \times 10^5$ S·m^{-1} in the range of 300–610 K, [33]). This phase seems to contribute most to the conduction of electrical current in those samples. Samples with lower Sb content (x = 0–0.19) display similar $\sigma(T)$ values, between $0.5 \times 10^4 - 1.3 \times 10^4$ S·m^{-1} after slow cooling and $0.4 \times 10^4 - 0.9 \times 10^4$ S·m^{-1} after quenching. The observed decrease of electrical conductivity after quenching (for x = 0–0.4) can be a consequence of pronounced carrier scattering, related to notable changes in the microstructure (Figure 4) and impurity concentration. It is also consistent with the decrease of charge carrier mobility (Figure 6a). It seems that mostly mobility influences σ values at T < 350 K. For x = 0.17, carrier concentrations of slowly cooled and quenched samples coincide with each other. It is worth highlighting the increase of carrier concentration with x (Figure 6b). Following the assumption that vacancies at 4*a* site are present in Ag-Sb-Te alloys and have an influence on hole concentration [25,27,28], the observed change in carrier concentration is expected. Low and high temperature data of σ perfectly coincide with each other, which proves the good homogeneity of the samples (inset in Figure 6a). At T < 200 K, σ is significantly increasing for x = 0.17, simultaneously with μ, and reaching the peak below 100 K (Figure 6a).

The temperature dependence of the Seebeck coefficient reflects that of electrical conductivity, and all alloys show *p*-type conductivity (Figure 5b). The lowest values were observed in alloys with x = 0.4 and 0.3 due to the precipitation Sb-Te phases. The other samples show higher Seebeck coefficients in the range of 200–375 μV·K^{-1}.

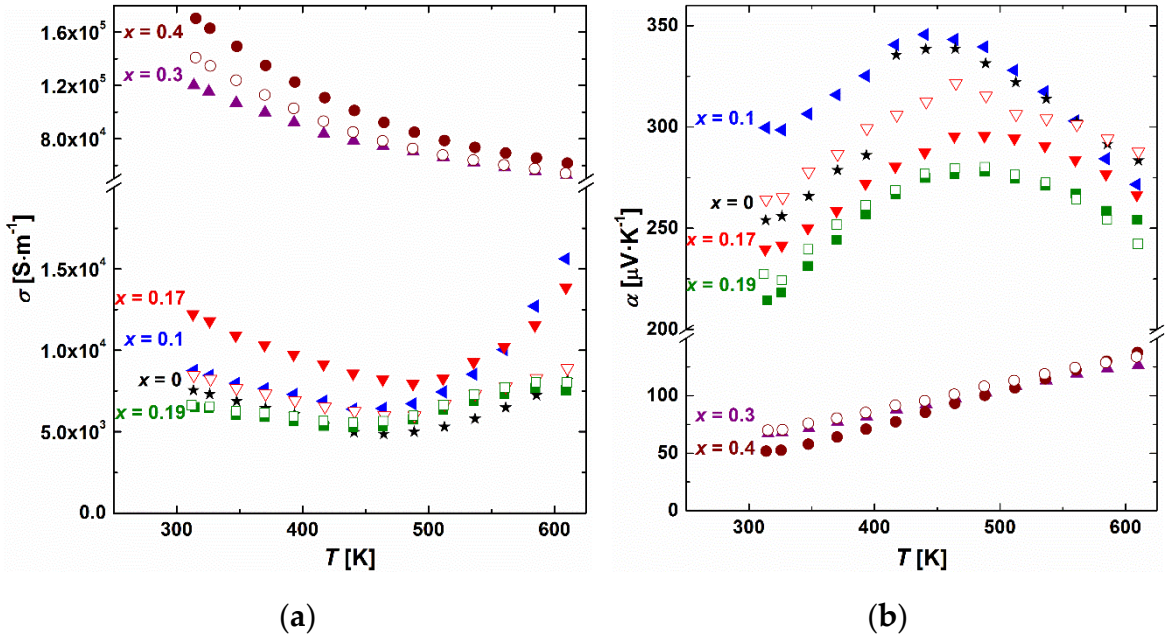

Figure 5. Temperature dependence of (**a**) electrical conductivity and (**b**) Seebeck coefficient of slowly cooled $Ag_{1-x}Sb_{1+x}Te_{2+x}$ samples (filled symbols). For comparison, data of three quenched samples are presented with open symbols (x = 0.4—circles, x = 0.19—squares, x = 0.17—triangles).

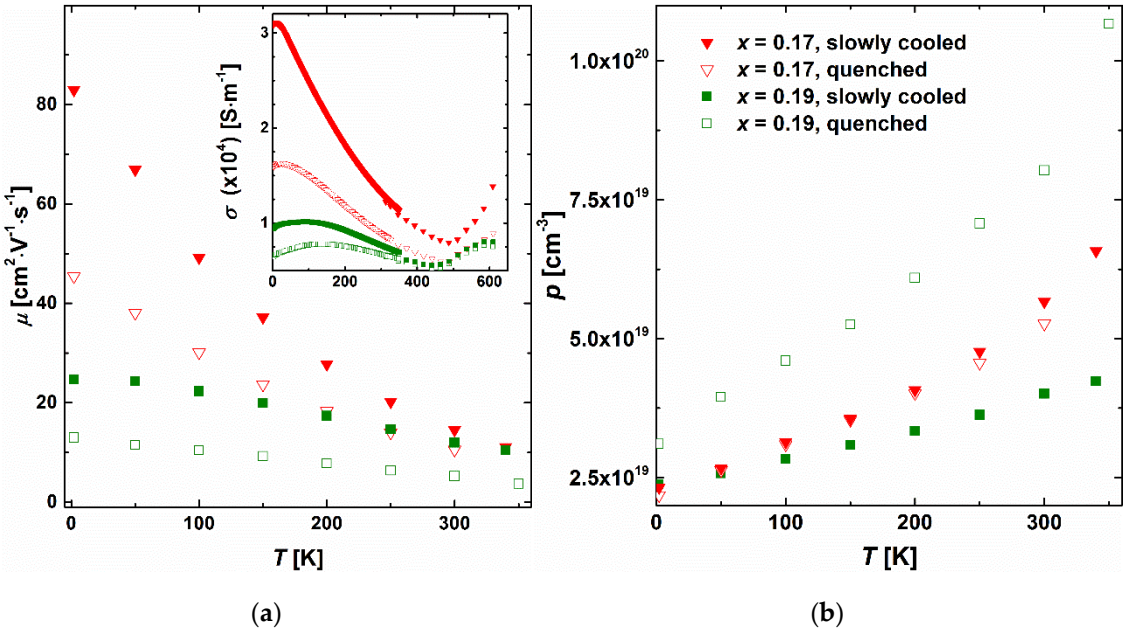

Figure 6. Temperature dependence of (**a**) charge carrier mobility and (**b**) charge carrier concentration for x = 0.17 (triangles), 0.19 (squares); inset in (**a**) presents temperature dependence of electrical conductivity in the range of 2–610 K; filled symbols—slowly cooled samples, open symbols—quenched samples.

Thermal conductivity as a function of temperature is presented in Figure 7a. The electronic contribution to thermal conductivity λ_e was calculated from the Wiedemann-Franz law $\lambda_e = L \cdot \sigma \cdot T$ (where $L = 2.44 \times 10^{-8}$ W·Ω·K^{-2} is the Lorenz number). The lattice part, containing also ambipolar contribution, was then determined by subtracting the electronic part from the total thermal conductivity. The highest values of thermal conductivity, 0.9–1.3 W·m^{-1}·K^{-1}, were observed for materials with a

notable concentration of Sb-Te impurities (x = 0.4 and 0.3), mainly due to their significant electronic contribution to heat conduction. However, the λ_e calculated from the Wiedemann-Franz law seems to be overestimated for these samples, resulting in very low lattice contribution (Figure 7b). The other alloys exhibit twice lower $\lambda(T)$ values, in the range of 0.4–0.7 $W \cdot m^{-1} \cdot K^{-1}$, similar to literature reports [7,26]. Lattice part is the main contribution to total thermal conductivity, independent of synthesis procedure (Figure 7b). Due to the included ambipolar part, values are slightly overestimated. Differences in thermal conductivity between samples after slow cooling and quenching, 5–10%, are on the level of measurement precision.

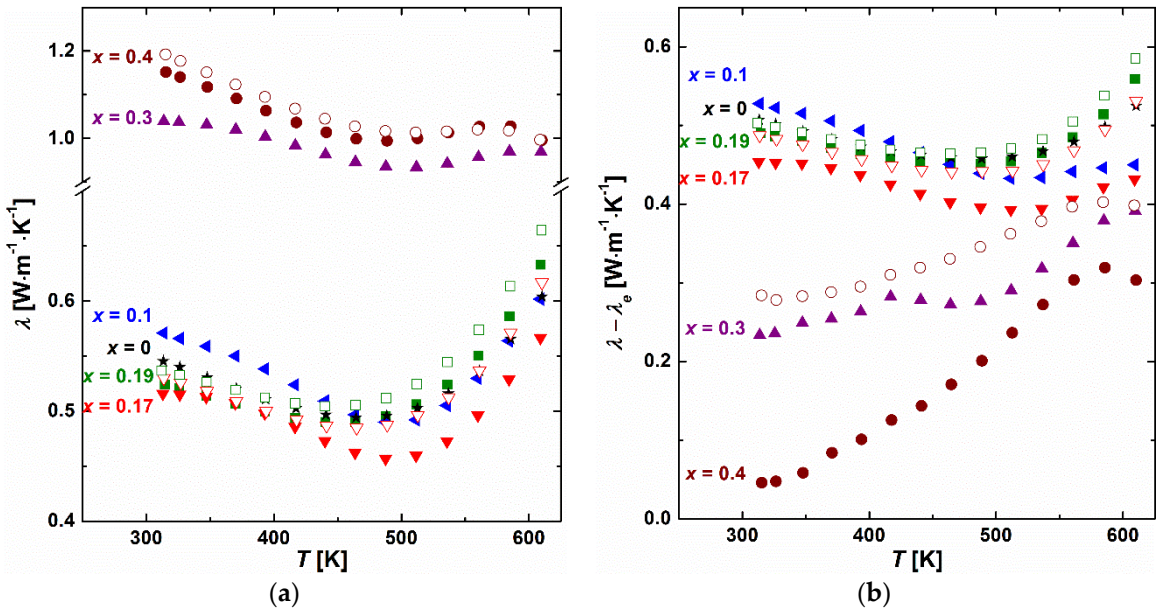

Figure 7. Temperature dependence of (**a**) total thermal conductivity and (**b**) its lattice contribution for slowly cooled $Ag_{1-x}Sb_{1+x}Te_{2+x}$ samples (filled symbols); for comparison, data of three quenched samples are presented with open symbols (x = 0.4—circles, x = 0.19—squares, x = 0.17—triangles).

One can notice extrema in the temperature dependence of Seebeck coefficient (maxima), electrical and thermal conductivity (minima), around 500 K that suggest an increase of the concentration of minority carriers—electrons, and an increase of their contribution to the electrical conductivity above 500 K. Such ambipolar conduction is observed in narrow-band-gap semiconductors [34]. Changes in the slope of $\alpha(T)$ and $\sigma(T)$ dependences at 420 K in Ag-rich alloys (x = 0, 0.1) are caused by polymorphic transition of Ag_2Te impurities [12,35].

The quality of synthesized materials was evaluated on the basis of the dimensionless thermoelectric figure of merit ZT (Figure 8). ZT grows monotonously with the temperature. Slowly cooled materials exhibit better TE performance compared to quenched samples. Slow cooling rate leads to crystallization of highly non-equilibrated alloys with a large number of defects and impurity phases, which effectively reduces lattice thermal conductivity. Samples x = 0.1 and x = 0.17 showed the highest values of ZT_{max}, 1.2 and 1.1 at 610 K, respectively.

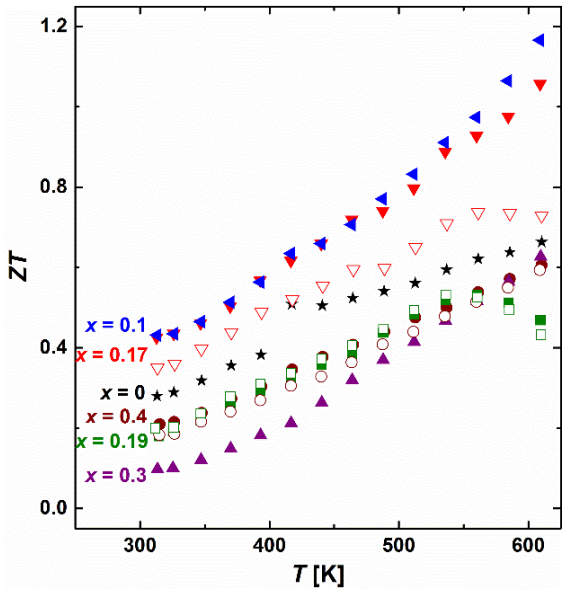

Figure 8. Temperature dependence of the figure of merit *ZT* for slowly cooled $Ag_{1-x}Sb_{1+x}Te_{2+x}$ samples (filled symbols); for comparison, data of three quenched samples are presented with open symbols (x = 0.4—circles, x = 0.19—squares, x = 0.17—triangles).

3.4. Intrinsic Properties of the β Phase ($Ag_{0.81}Sb_{2.19}Te_{2.19}$)

As it was shown in previous paragraphs, the majority of $Ag_{1-x}Sb_{1+x}Te_{2+x}$ alloys are multi-phase. Thus, measured physical properties reflect the intrinsic properties of the β phase, defect arrangement and the impurity phases. That is why it is not reasonable to present the dependence of TE properties versus lattice parameter or chemical composition. Intrinsic properties of the β phase were described for the quenched alloy with x = 0.19 only. No secondary phases were detected in this sample, within the precision of PXRD (Figure 9a) or SEM analysis (Figure 9b).

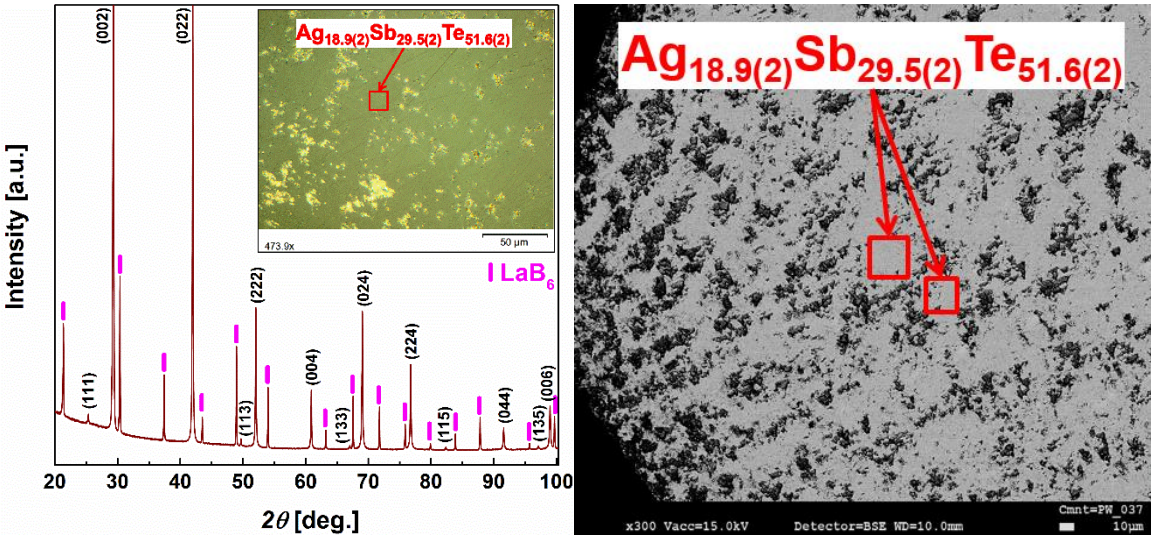

(**a**) (**b**)

Figure 9. PXRD and microstructure characterization of the quenched sample with x = 0.19: (**a**) Powder XRD pattern; LaB_6 was used as an internal standard; inset: optical polarized light micrograph; (**b**) Backscattered-electron (BSE) image with chemical composition according to EDXS analysis.

Electrical conductivity, Seebeck coefficient and total thermal conductivity in the temperature range of 300–610 K equal $5.5 \times 10^3 - 8 \times 10^3$ S·m, 220–280 μV·K^{-1} and 0.55–0.65 W·m^{-1}·K^{-1}, respectively (Figure 10a,b). The dependences $\sigma(T)$. $\alpha(T)$ and $\lambda(T)$ show extrema, suggesting ambipolar conduction to be an intrinsic property of the β phase. Charge carrier concentration is increasing from 3×10^{19} to 1×10^{20} at low temperatures (3–350 K, Figure 6b). Lattice contribution (together with ambipolar part) to thermal conductivity is higher than 90% of total λ, showing that phonon propagation processes limit the conduction of heat in the β phase (Figure 10b). The highest ZT_{max} value equals 0.4 at 550 K (Figure 8).

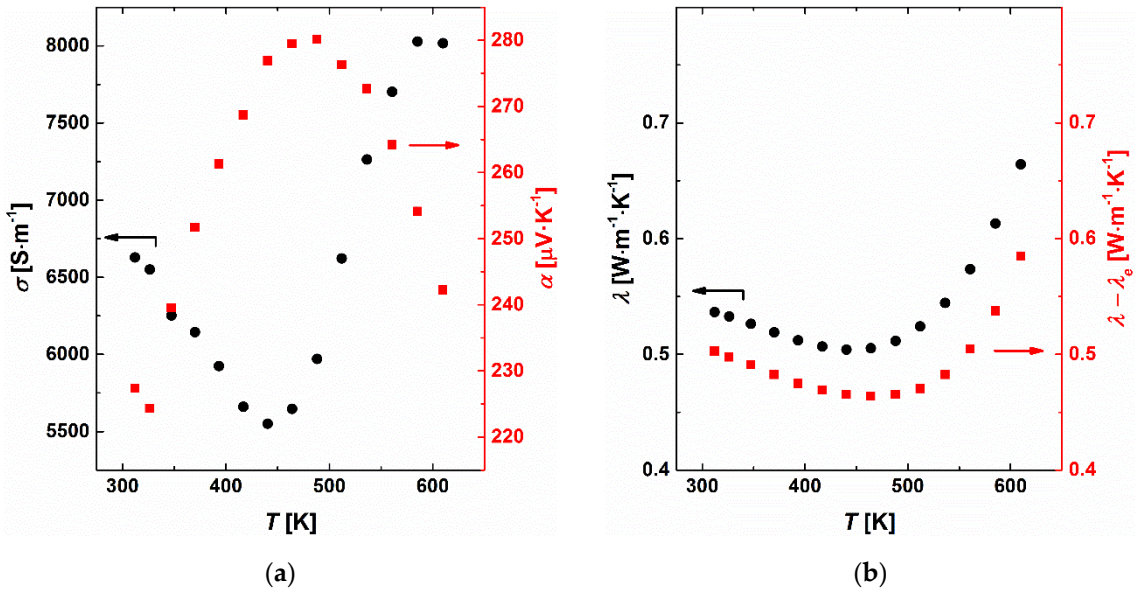

Figure 10. Thermoelectric properties of the quenched $x = 0.19$ sample as a function of temperature: (**a**) Electrical conductivity and Seebeck coefficient; (**b**) Total thermal conductivity and its lattice contribution.

3.5. Nanostructure of the β Phase ($Ag_{0.81}Sb_{1.19}Te_{2.19}$)

Nanostructure usually affects electronic transport properties of TE materials [34]. In the case of Ag-Sb-Te-based alloys, the presence of point and linear defects, together with different nanodomains, are believed to effectively suppress thermal conductivity to theoretically minimal values [9,15,25].

In this study, we performed a thorough analysis of a quenched $Ag_{0.81}Sb_{1.19}Te_{2.19}$ alloy ($x = 0.19$), by means of transmission electron microscopy (TEM) and selected area electron diffraction (SAED). As mentioned in the previous paragraph, the influence of a possible impurity phase on the nanostructure of this sample is minimal if any. We present, in detail, two representative particles: particle I (Figure 11a–d and Figure S6) and particle II (Figure 12a–d) with ~0.5 μm and ~2 μm size, respectively. SAED pattern ([110] zone axis) for the whole particle I consists of sharp reflections that belong to the NaCl structure type only (inset in Figure 11a). Interplanar distances for $(2\bar{2}0)$ and (002) planes are in good agreement with values refined from PXRD data for $Ag_{0.81}Sb_{1.19}Te_{2.19}$ (2.15 Å and 3.04 Å respectively). Under higher magnification (~40 × 40 nm field of view), well-ordered structure is visible with sharp reflections in the fast Fourier transform (FFT) pattern and correct interplanar distances (Figure S6). The well-ordered atomic arrangement within (110) plane is presented in detail in the high-resolution (HRTEM) image (Figure 11b) and is compared to the NaCl type structure model. The lattice parameter is in agreement (within the experimental error) with PXRD data. Interestingly, the chemical composition of particle I is $Ag_{23(1)}Sb_{28(1)}Te_{49(1)}$, according to EDXS analysis, and reveals a small excess of Ag, compared to the nominal composition $Ag_{19}Sb_{29}Te_{52}$. The FFT pattern from some regions of particle I contains additional reflections indicating doubling of the unit cell along

[111] direction (Inset in Figure 11c). The doubling effect is clearly visible in Bragg-filtered IFFT image composed only from additional reflections along [111] direction (Figure 11d). Irregular nanodomains with well-ordered atomic arrangement (marked with dashed lines in Figure 11d) are surrounded by distorted regions. It is similar to the previously predicted and observed segregation of Ag/Sb atoms to alternating (111) planes [9,18]. However, such forbidden reflections can also be visible due to multiple scattering processes during TEM observations.

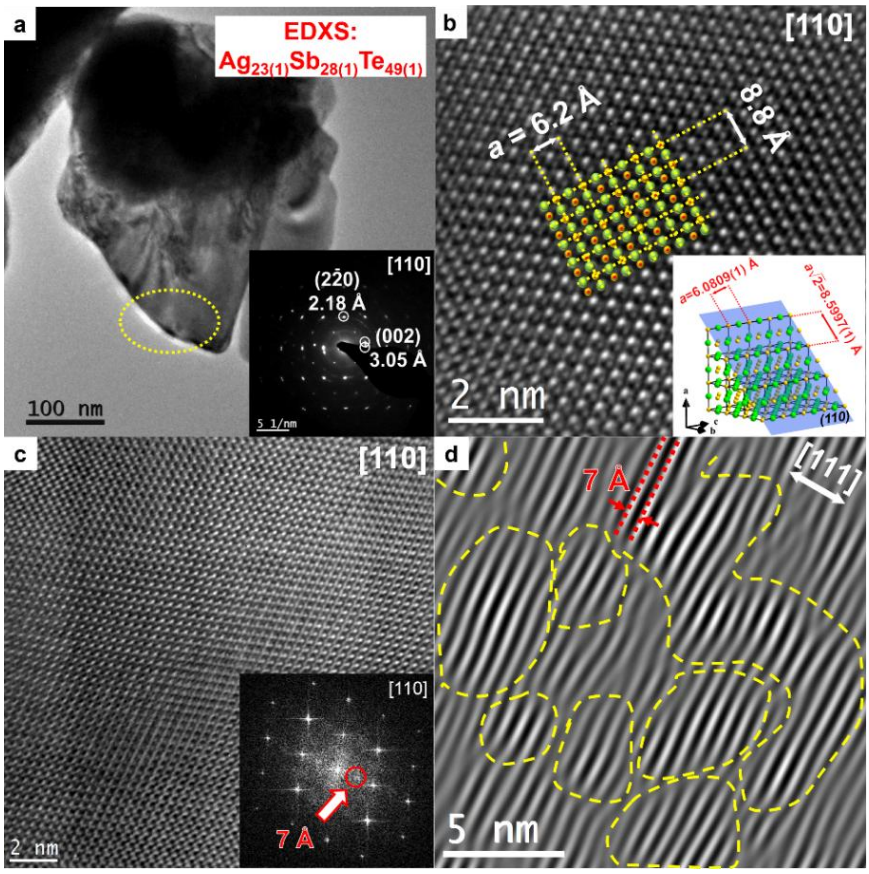

Figure 11. TEM analysis for particle I of quenched $Ag_{19}Sb_{29}Te_{52}$ sample (x = 0.19): (**a**) Particle I together with chemical composition according to EDXS analysis. Inset: an SAED pattern from the whole particle I. Doubling of each reflection is the result of rotated second crystal below; (**b**) HRTEM image of a selected area within particle I (yellow dotted circle in Figure 11a) compared with unit cell cross section along [110] plane and lattice parameter refined from PXRD (inset); (**c**) FFT filtered HR image of another region of particle I. The FFT pattern contains additional reflections, with an interplanar distance of 7 Å, which indicate doubling of the unit cell along [111] direction (inset); (**d**) Bragg-filtered IFFT image composed only from additional reflections along [111] direction. Stripe pattern corresponds to crystallographic planes normal to [111] direction with period equals 7 Å.

Particle II shows a gradual increase in the level of atomic disorder. Sharp reflections of NaCl type structure are becoming diffuse, while increasing magnification from the entire particle II to smaller regions (Figure 12a–c). Two scenarios were observed: (i) intermediate state with co-existence of large well-ordered and disordered regions (Figure 12b). FFT patterns ([110] zone axis), from both regions, comprise diffuse NaCl type reflections (insets in Figure 12b). (ii) Mosaic pattern with alternating ordered and disordered nanodomains (~2–5 nm) (Figure 12c,d). Additional reflections are distinguishable for the disordered region (yellow circles in FFT in Figure 12c), caused by similar orientation of nanograins with disturbed crystal lattices. Interplanar distances are larger than the theoretical values for the cubic structure, particularly in the disordered domains (inset FFT in

Figure 12c). An average chemical composition of particle II is $Ag_{22(1)}Sb_{24(1)}Te_{54(1)}$, according to EDXS. Excess of Ag and deficiency of Sb was observed, in respect to the nominal composition $Ag_{19}Sb_{29}Te_{52}$.

It seems that the synthesis conditions prevent equilibration of the β phase and obtained materials consist of grains with deviated composition. The co-existence of the well-ordered and the disordered nanodomains together with the variation in the chemical composition have a strong influence on the formation of the particular nanostructure that is very favorable for phonon scattering and minimization of lattice thermal conductivity [9,36].

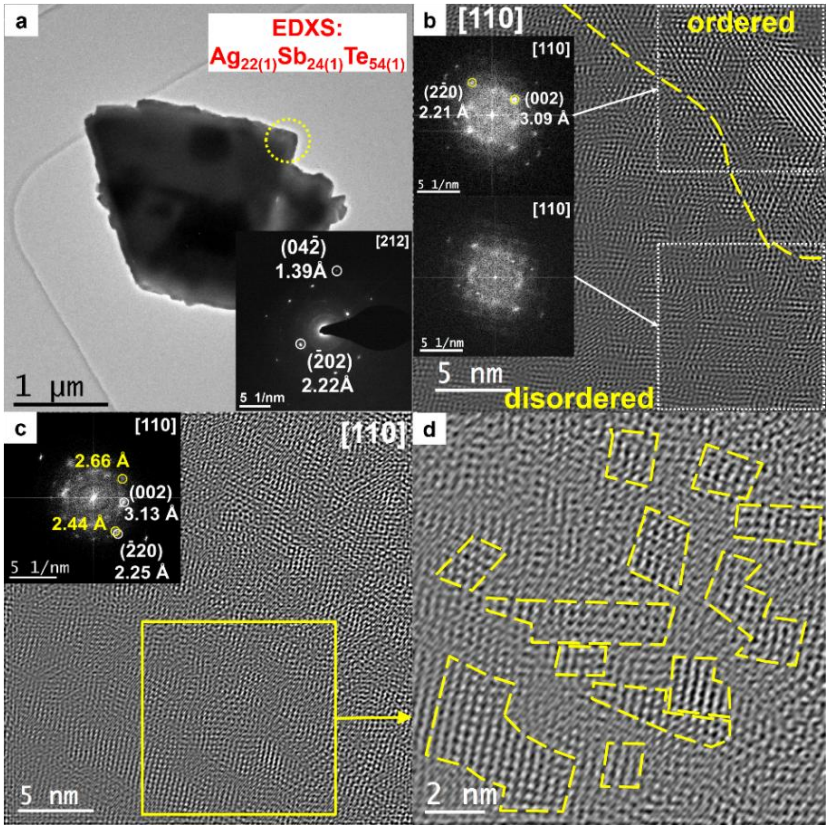

Figure 12. TEM analysis of particle II of quenched $Ag_{19}Sb_{29}Te_{52}$ sample (x = 0.19): (**a**) Particle II together with chemical composition according to EDXS analysis. Inset: an SAED pattern from the whole particle I; (**b**) FFT filtered HR image of region 1 within particle II. It consists of disordered (mosaic) and ordered parts. Insets: FFT patterns ([110] zone axis), from both analyzed areas; (**c**) FFT filtered HR image of region 2 within particle II shows mosaic pattern only. Inset: FFT pattern from the whole region in Figure 12c; (**d**) Magnified HR image of area marked with the yellow square in Figure 12c. Well-ordered nanograins (marked with dashed lines) are surrounded by disordered domains.

3.6. Thermodynamic Stability

The eutectoid decomposition of the β phase below 633 K significantly affects TE properties of $Ag_{1-x}Sb_{1+x}Te_{2+x}$ alloys [12]. One representative quenched alloy, x = 0.1, was chosen to show the degradation during the physical measurements below the formation/decomposition temperature of the β phase (Figure 13). Electrical conductivity values are reproducible up to 490 K (black squares in figure caption) and then monotonously increasing during the following measurements (heating-cooling part), from 5 × 10^3 to 30 × 10^3 S·m^{-1} at 310 K (Figure 13a). The gradual decrease of the Seebeck coefficient is visible, from 346 to 195 μV·K^{-1} at 310 K (Figure 13b). It is a result of the formation of Sb-Te impurities (Figure 13d), which strongly influence the TE properties of Ag-Sb-Te alloys (compare Figures 5–8). A slight increase in thermal conductivity was observed below 530 K even after one

measurement cycle (Figure 13c). After the 7th measurement at the ZEM apparatus, λ increases by 35%, reaching 0.67 $W \cdot m^{-1} \cdot K^{-1}$ at *RT*. The discrepancies between subsequent measurements become notable in the range of 490–535 K. It leads to the conclusion that the decomposition rate of the β phase increases significantly at about 100–140 K below the decomposition temperature. Interestingly, *ZT* parameter at *RT* after seven measurements remains unchanged, due to significant increase of σ. All studied $Ag_{1-x}Sb_{1+x}Te_{2+x}$ alloys (x = 0; 0.1; 0.17, 0.19, 0.3, 0.4) reveal presented behavior. Considering TE properties only, the experiment leads to the conclusion that Ag-Sb-Te-based materials could be utilized in TE devices working up to 490 K.

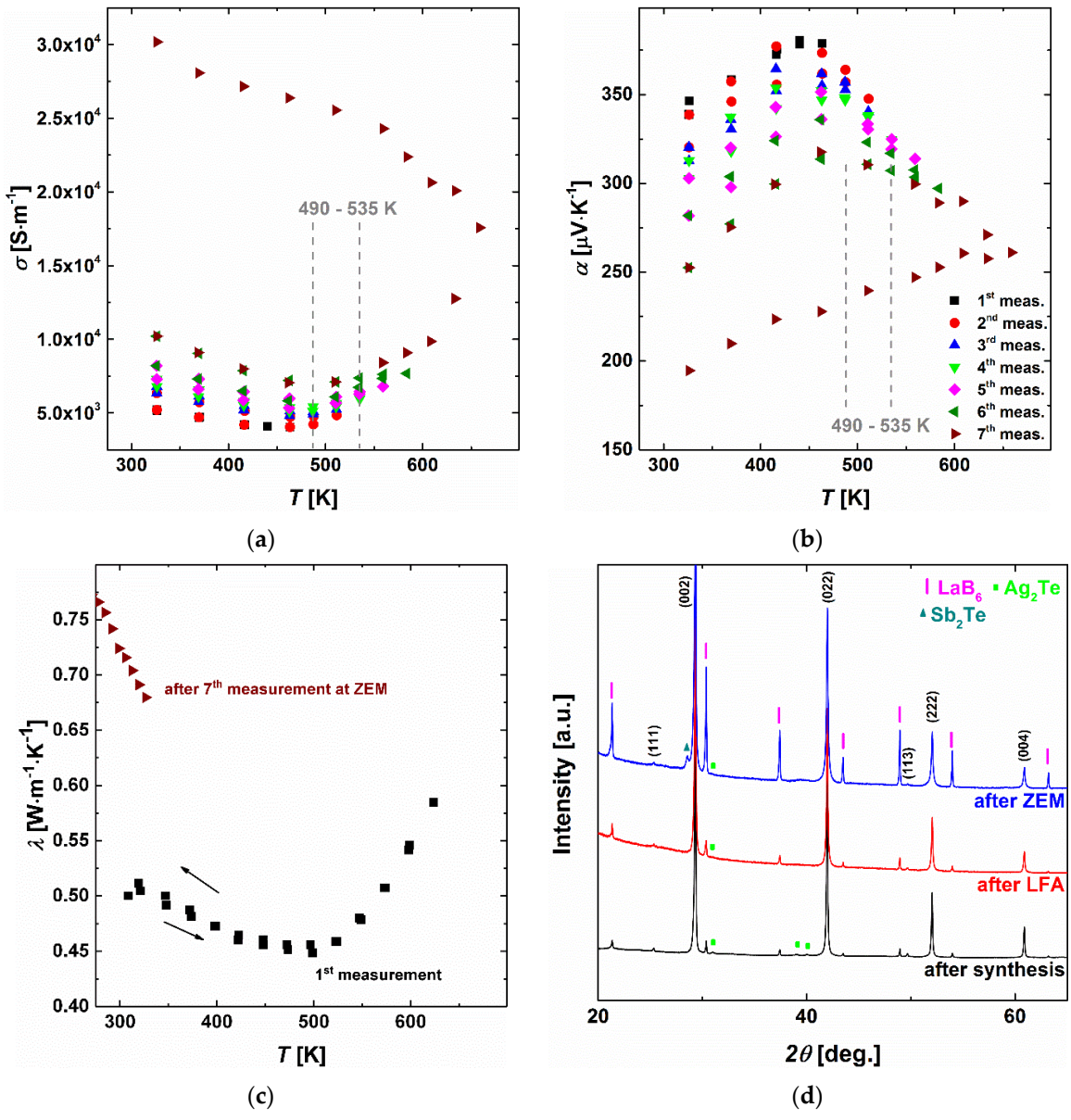

Figure 13. Thermoelectric and PXRD characterization of the quenched $Ag_{0.9}Sb_{1.1}Te_{2.1}$ sample after sequential measurements: (**a**) Electrical conductivity; (**b**) Seebeck coefficient; (**c**) Thermal conductivity; (**d**) PXRD patterns.

4. Conclusions

Two series of $Ag_{1-x}Sb_{1+x}Te_{2+x}$ samples (x = 0; 0.1; 0.17; 0.19; 0.3; 0.4) were synthesized utilizing slow cooling and quenching. All obtained materials reveal *p*-type conductivity with a metal-like

temperature dependence of the electrical conductivity up to 500 K. Their TE properties strongly depend on the concentration of secondary phases and features of the microstructure. A higher cooling rate suppressed crystallization of secondary phases and enabled to obtain single-phase material only with $x = 0.19$. Due to the decrease in solidification time, the quenching procedure disrupts the formation of microstructures improving TE properties. Therefore, we regard $Ag_{1-x}Sb_{1+x}Te_{2+x}$ alloys as: (i) the multi-phase materials and (ii) the materials with TE properties resulting from the combination of intrinsic properties of the β phase (e.g., $x = 0.19$) and minority phases. High level of disorder in nanoscale in the β phase was observed in TEM, including mosaic patterns and disorientation of grains. It plays an important role in the reduction of lattice thermal conductivity. Slowly cooled alloys with $x = 0.1$ and $x = 0.17$ exhibit the highest TE performance, showing ZT values of 1.2 and 1.1 at 610 K, respectively. It is clear that high ZT values in $Ag_{1-x}Sb_{1+x}Te_{2+x}$ alloys can also be obtained without extrinsic doping as reported previously [2–6]. All samples reveal lack of long-term stability, which causes degradation of the β phase and the TE performance, in agreement with the phase diagram of the Ag-Sb-Te system. However, TE properties are reproducible up to 490 K due to kinetic hindering of the eutectoid decomposition of the β phase. $Ag_{1-x}Sb_{1+x}Te_{2+x}$ alloys show more favorable TE properties than alloys with a nominal composition $Ag_{1.0}Sb_{1.0}Te_{2.0}$. To utilize them, the suppression of the eutectoid decomposition is needed, probably by chemical substitution.

Supplementary Materials: The following are available online at http://www.mdpi.com/2076-3417/8/1/52/s1, Figure S1: (a) TG-DTA analysis of slowly cooled $Ag_{1.0}Sb_{1.0}Te_{2.0}$ and (b) DTA analysis of slowly-cooled $Ag_{0.81}Sb_{1.19}Te_{2.19}$ samples; Table S1: Thermal effects observed in DTA curves with corresponding reactions; Figure S2: Optical micrographs of $Ag_{0.6}Sb_{1.4}Te_{2.4}$ and $Ag_{0.81}Sb_{1.19}Te_{2.19}$ samples; Figures S3 and S4: Backscattered-electron (BSE) images of the $Ag_{1-x}Sb_{1+x}Te_{2+x}$ samples; Figure S5: Real element concentration of: (a) Ag, (b) Sb, (c) Te as a function of nominal concentration in the $Ag_{1-x}Sb_{1+x}Te_{2+x}$ samples; Figure S6: HRTEM image of particle I of $Ag_{19}Sb_{29}Te_{52}$ sample ($x = 0.19$).

Acknowledgments: The authors thank members of competence group Structure (MPI CPfS) for PXRD analysis, Markus Schmidt (MPI CPfS) for TG-DSC measurements, Gudrun Auffermann (MPI CPfS) for chemical analysis and Matej Bobnar for low-temperature thermoelectric measurements. This work was partially supported by the funds of National Science Center Poland granted on the basis of the decision No. DEC-2013/09/B/ST8/02043.

Author Contributions: Krzysztof T. Wojciechowski and Yuri Grin initiated the idea of the research. Paweł Wyżga and Igor Veremchuk performed synthesis, measurements of transport properties and evaluation of data. Ulrich Burkhardt analyzed the microstructure. Paul Simon performed the TEM studies. Paweł Wyżga prepared manuscript.

Conflicts of Interest: The authors declare no conflict of interest.

References

1. Tritt, T.M. Thermoelectric phenomena, materials, and applications. *Annu. Rev. Mater. Res.* **2011**, *41*, 433–448. [CrossRef]
2. Roychowdhury, S.; Panigrahi, R.; Perumal, S.; Biswas, K. Ultrahigh thermoelectric figure of merit and enhanced mechanical stability of p-type $AgSb_{1-x}Zn_xTe_2$. *ACS Energy Lett.* **2017**, *2*, 349–356. [CrossRef]
3. Schmidt, M.; Wojciechowski, K.T. Reinvestigation of the influence of Se impurity on the structural and thermoelectric properties of $AgSbTe_2$. *AIP Conf. Proc.* **2012**, *1449*, 175–178. [CrossRef]
4. Du, B.; Li, H.; Xu, J.; Tang, X.; Uher, C. Enhanced figure-of-merit in Se-doped p-type $AgSbTe_2$ thermoelectric compound. *Chem. Mater.* **2010**, *22*, 5521–5527. [CrossRef]
5. Wu, H.J.; Lan, T.W.; Chen, S.W.; Chen, Y.Y.; Day, T.; Snyder, G.J. State of the art $Ag_{50-x}Sb_xSe_{50-y}Te_y$ alloys: Their high ZT values, microstructures and related phase equilibria. *Acta Mater.* **2015**, *93*, 38–45. [CrossRef]
6. Mohanraman, R.; Sankar, R.; Boopathi, K.M.; Chou, F.C.; Chu, C.W.; Lee, C.H.; Chen, Y.-Y. Influence of In doping on the thermoelectric properties of an $AgSbTe_2$ compound with enhanced figure of merit. *J. Mater. Chem. A* **2014**, *2*, 2839–2844. [CrossRef]
7. Morelli, D.T.; Jovovic, V.; Heremans, J.P. Intrinsically minimal thermal conductivity in cubic I-V-VI_2 semiconductors. *Phys. Rev. Lett.* **2008**, *101*, 035901. [CrossRef] [PubMed]
8. Du, B.; Chen, K.; Yan, H.; Reece, M.J. Efficacy of lone-pair electrons to engender ultralow thermal conductivity. *Scr. Mater.* **2016**, *111*, 49–53. [CrossRef]

9. Ma, J.; Delaire, O.; May, A.F.; Carlton, C.E.; Mcguire, M.A.; VanBebber, L.H.; Abernathy, D.L.; Ehlers, G.; Hong, T.; Huq, A.; et al. Glass-like phonon scattering from a spontaneous nanostructure in $AgSbTe_2$. *Nat. Nanotechnol.* **2013**, *8*, 445–451. [CrossRef] [PubMed]
10. Petzow, G.; Effenberg, G. *Ternary Alloys: A Comprehensive Compendium of Evaluated Constitutional Data and Phase Diagrams*; Wileys-VCH Verlag: Weinheim, Germany, 1998; pp. 552–554, ISBN 3-527-26967-3.
11. Wu, H.J.; Chen, S.W. Phase equilibria of Ag-Sb-Te thermoelec tric materials. *Acta Mater.* **2011**, *59*, 6463–6472. [CrossRef]
12. Wyzga, P.M.; Wojciechowski, K.T. Analysis of the influence of thermal treatment on the stability of $Ag_{1-x}Sb_{1+x}Te_{2+x}$ and Se-doped $AgSbTe_2$. *J. Electron. Mater.* **2016**, *45*, 1548–1554. [CrossRef]
13. Wernick, J.H.; Benson, K.E. New semiconducting ternary compounds. *J. Phys. Chem. Solids* **1957**, *3*, 157–159. [CrossRef]
14. Geller, S.; Wernick, J.H. Ternary semiconducting compounds with sodium chloride-like structure: $AgSbSe_2$, $AgSbTe_2$, $AgBiS_2$, $AgBiSe_2$. *Acta Crystallogr.* **1959**, *12*, 46–54. [CrossRef]
15. Quarez, E.; Hsu, K.F.; Pcionek, R.; Frangis, N.; Polychroniadis, E.K.; Kanatzidis, M.G. Nanostructuring, compositional fluctuations, and atomic ordering in the thermoelectric materials $AgPb_mSbTe_{2+m}$. The myth of solid solutions. *J. Am. Chem. Soc.* **2005**, *127*, 9177–9190. [CrossRef] [PubMed]
16. Wojciechowski, K.; Toboła, J.; Schmidt, M.; Zybała, R. Structural and thermoelectric properties of $AgSbSe_2$ and $AgSbTe_2$. In Proceedings of the 5th European Conference on Thermoelectrics (ECT2007), Odessa, Ukraine, 10–12 September 2007.
17. Rezaei, N.; Hashemifar, S.J.; Akbarzadeh, H. Thermoelectric properties of $AgSbTe_2$ from first-principles calculations. *J. Appl. Phys.* **2014**, *116*, 103705. [CrossRef]
18. Hoang, K.; Mahanti, S.D.; Salvador, J.R.; Kanatzidis, M.G. Atomic ordering and gap formation in Ag-Sb-based ternary chalcogenides. *Phys. Rev. Lett.* **2007**, *99*, 156403. [CrossRef] [PubMed]
19. Marin-Ayral, R.M.; Legendre, B.; Brun, G.; Liautard, B.; Tedenac, J.C. The ternary system silver-antimony-tellurium. Study of the subternary Sb_2Te_3-Ag_2Te-Te. *Thermochim. Acta* **1988**, *131*, 37–45. [CrossRef]
20. Wojciechowski, K.T.; Schmidt, M. Structural and thermoelectric properties of $AgSbTe_2$-$AgSbSe_2$ pseudobinary system. *Phys. Rev. B* **2009**, *79*, 184202. [CrossRef]
21. Du, B.; Yan, Y.; Tang, X. Variable-temperature in situ X-ray diffraction study of the thermodynamic evolution of $AgSbTe_2$ thermoelectric compound. *J. Electron. Mater.* **2015**, *44*, 2118–2123. [CrossRef]
22. Aspiala, M.; Taskinen, P. Thermodynamic study of the Ag-Sb-Te system with an advanced EMF method. *J. Chem. Thermodyn.* **2016**, *93*, 261–266. [CrossRef]
23. Armstrong, R.W.; Faust, J.W., Jr.; Tiller, W.A. A structural study of the compound $AgSbTe_2$. *J. Appl. Phys.* **1960**, *31*, 1954–1959. [CrossRef]
24. Matsushita, H.; Hagiwara, E.; Katsui, A. Phase diagram and thermoelectric properties of $Ag_{3-x}Sb_{1+x}Te_4$ system. *J. Mater. Sci.* **2004**, *39*, 6299–6301. [CrossRef]
25. Zhang, S.N.; Zhu, T.J.; Yang, S.H.; Yu, C.; Zhao, X.B. Phase compositions, nanoscale microstructures and thermoelectric properties in $Ag_{2-y}SbyTe_{1+y}$ alloys with precipitated Sb_2Te_3 plates. *Acta Mater.* **2010**, *58*, 4160–4169. [CrossRef]
26. Nielsen, M.D.; Jaworski, C.M.; Heremans, J.P. Off-stoichiometric silver antimony telluride: An experimental study of transport properties with intrinsic and extrinsic doping. *AIP Adv.* **2015**, *5*, 053602. [CrossRef]
27. Jovovic, V.; Heremans, J.P. Measurements of the energy band gap and valence band structure of $AgSbTe_2$. *Phys. Rev. B* **2008**, *77*, 245204. [CrossRef]
28. Jung, H.; Park, H.; Choa, Y.; Myung, N.V. Composition-dependent electrical properties of ternary $Ag_xSb_{1-x}Te_y$ thin films synthesized by cationic exchange reaction. *Electron. Mater. Lett.* **2012**, *8*, 219–224. [CrossRef]
29. Akselrud, L.; Grin, Y. WinCSD: Software package for crystallographic calculations (Version 4). *J. Appl. Crystallogr.* **2014**, *47*, 803–805. [CrossRef]
30. Max-Planck-Institut für Chemische Physik fester Stoffe. *Scientific Report 2006–2008*; Max-Planck-Institut für Chemische Physik Fester Stoffe: Dresden, Germany, 2009.
31. Karakaya, I.; Thompson, W.T. The Ag-Te (silver-tellurium) system. *J. Phase Equilib.* **1991**, *12*, 56–63. [CrossRef]

32. Cojocaru-Miredin, O.; Abdellaoui, L.; Nagli, M.; Zhang, S.; Yu, Y.; Scheu, C.; Raabe, D.; Wuttig, M.; Amouyal, Y. Role of nanostructuring and microstructuring in silver antimony telluride compounds for thermoelectric applications. *ACS Appl. Matter. Interfaces* **2017**, *9*, 14779–14790. [CrossRef] [PubMed]
33. Roy, B.; Chakraborty, B.R.; Bhattacharya, R.; Dutta, A.K. Electrical and magnetic properties of antimony telluride. *Solid State Commun.* **1978**, *25*, 617–620. [CrossRef]
34. Goldsmid, H.J. *Introduction to Thermoelectricity*, 1st ed.; Springer: Berlin/Heidelberg, Germany, 2010; p. 203, ISBN 978-3-642-00715-6.
35. Ragimov, S.S.; Aliev, S.A. $\alpha \rightarrow \beta$ phase transition of Ag_2Te in the $AgSbTe_2$ alloy of the Ag-Sb-Te system. *Inorg. Mater.* **2007**, *43*, 1184–1186. [CrossRef]
36. Biswas, K.; He, J.; Blum, I.D.; Wu, C.I.; Hogan, T.P.; Seidman, D.N.; Dravid, V.P.; Kanatzidis, M.G. High-performance bulk thermoelectrics with all-scale hierarchical architectures. *Nature* **2012**, *489*, 414–418. [CrossRef] [PubMed]